Image-Guided Navigation of a Robotic Ultrasound Probe for Autonomous Spinal Sonography Using a Shadow-aware Dual-Agent Framework

Keyu Li, Yangxin Xu, Jian Wang, Dong Ni, Li Liu*, and Max Q.-H. Meng*, *Fellow*, *IEEE*

***Abstract*—Ultrasound (US) imaging is commonly used to assist in the diagnosis and interventions of spine diseases, while the standardized US acquisitions performed by manually operating the probe require substantial experience and training of sonographers. In this work, we propose a novel dual-agent framework that integrates a reinforcement learning (RL) agent and a deep learning (DL) agent to jointly determine the movement of the US probe based on the real-time US images, in order to mimic the decision-making process of an expert sonographer to achieve autonomous standard view acquisitions in spinal sonography. Moreover, inspired by the nature of US propagation and the characteristics of the spinal anatomy, we introduce a view-specific acoustic shadow reward to utilize the shadow information to implicitly guide the navigation of the probe toward different standard views of the spine. Our method is validated in both quantitative and qualitative experiments in a simulation environment built with US data acquired from 17 volunteers. The average navigation accuracy toward different standard views achieves $5.18mm/5.25^\circ$ and $12.87mm/17.49^\circ$ in the intra- and inter-subject settings, respectively. The results demonstrate that our method can effectively interpret the US images and navigate the probe to acquire multiple standard views of the spine.**

***Index Terms*—Medical robotic system, Robot decision-making, Robotic ultrasound, Ultrasound image analysis.**

I. Introduction

MEDICAL ultrasound (US) imaging has been widely accepted in a broad range of clinical applications because of its ease of use, non-invasiveness, low cost and real-time capabilities. In spinal applications, US imaging is a commonly practiced diagnostic tool for various spine diseases such as scoliosis and low-back pain [1], and is also frequently used in preprocedural scan [2] and real-time needle guidance during minimally invasive spine procedures [3][4].

This work was partially supported by National Key R&D program of China with Grant No. 2019YFB1312400, Hong Kong RGC GRF grant #14210117, Hong Kong RGC TRS grant T42-409/18-R and Hong Kong RGC GRF grant #14211420 awarded to Max Q.-H. Meng.

K. Li, Y. Xu and L. Liu are with the Department of Electronic Engineering, The Chinese University of Hong Kong, Hong Kong, China (e-mail: kyli@link.cuhk.edu.hk; yxxu@link.cuhk.edu.hk; liliu@cuhk.edu.hk).

J. Wang and D. Ni are with the School of Biomedical Engineering, Shenzhen University, Shenzhen, China. (e-mail: wangjian2018@email.szu.edu.cn; nidong@szu.edu.cn).

Max Q.-H. Meng is with the Department of Electronic and Electrical Engineering of the Southern University of Science and Technology in Shenzhen, China, on leave from the Department of Electronic Engineering, The Chinese University of Hong Kong, Hong Kong, and also with the Shenzhen Research Institute of the Chinese University of Hong Kong in Shenzhen, China (e-mail: max.meng@ieee.org).

*Corresponding authors.

In standardized US acquisitions, the *standard views* are a number of view planes defined by expert consensus to perform US imaging of specific anatomical structures, which usually contain essential information of the anatomy for diagnosis, biometric measurement or interventional guidance [5][6]. For example, an overview of the lumbar spine anatomy is show in Fig. 1(a). Each lumbar vertebra is composed of a vertebral body, a spinous process, two laminae, two transverse processes, two articular processes and two pedicles [7]. The US examination of the lumbar spine typically involves the imaging of three standard views, namely, the *paramedian sagittal lamina* (PSL) view, *paramedian sagittal articular processes* (PSAP) view, and *transverse spinous process* (TSP) view [8][9], as illustrated in Fig. 1(b). The PSL and PSAP views can be acquired during the paramedian sagittal scan at the level of the lamina and articular process, respectively, and the TSP view is acquired during the transverse scan when the probe is placed over the spinous process. Acquiring these standard views can help the physician identify and locate the spinal anatomical landmarks to perform diagnosis or spine procedures [7].

However, the current standard view acquisition procedure requires manual navigation of the probe based on the interpretation of the US images and the knowledge of the internal anatomy, which usually requires substantial experience and extensive training of sonographers. Therefore, the sonographers are suffering from heavy physical and cognitive burdens due to excessive workload [10], and the imaging quality is strongly dependent on the operator [11]. In addition, the direct patient contact would increase the risk of infection for frontline medical staff during a pandemic such as COVID-19 [12]. In view of this, an autonomous robotic system for US acquisitions holds great promise for relieving user workload, improving imaging results, and reducing the need for direct patient contact [13].

Autonomously navigating the US probe toward the standard view is a highly challenging task, as it requires the robot to interpret the US image data and perform visual navigation, which mimics the decision-making process of an experienced sonographer. As an active field of research in artificial intelligence, reinforcement learning (RL) has become a powerful tool for solving complex sequential decision-making problems in real-world applications [14]. Meanwhile, deep learning (DL) has superior ability in learning high-level representation from raw image data and has been intensively studied in US image analysis tasks [15]. Therefore, a combination of RL and

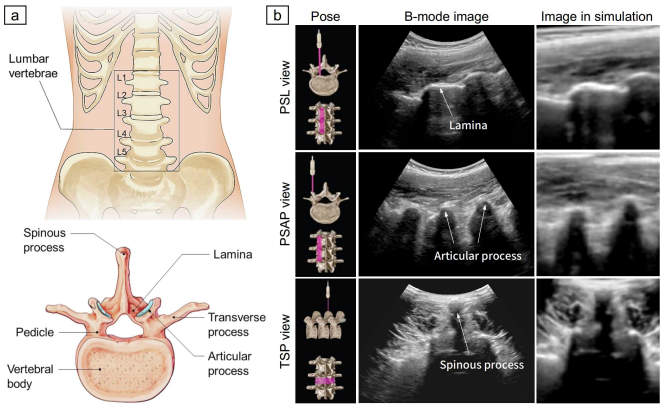

Fig. 1. (a) Lumbar spine anatomy and (b) US acquisitions of three standard views of the lumbar spine, i.e., PSL: paramedian sagittal lamina view, PSAP: paramededian sagittal articular process view, and TSP: transverse spinal process view of the spine. The left column illustrates the corresponding probe poses [7]. The middle column presents the B-mode images acquired by a clinician from a volunteer. The right column shows the corresponding images acquired with the same probe poses from the virtual patient in our simulation.

DL techniques can be a potential solution to our problem.

In this paper, we introduce a novel framework that integrates RL and DL techniques to achieve autonomous standard view acquisitions in robotic spinal sonography. An overview showing the main components of our proposed framework is illustrated in Fig. 2. An RL agent for navigation action selection and a DL agent for standard view recognition are proposed to jointly determine the movement of the probe to search for the standard views of the spine. Furthermore, inspired by the nature of US propagation and the characteristics of the spinal anatomy, we introduce a novel approach to utilize the acoustic shadow information in the learning of navigation policy. The main contributions of this paper are as follows.

- A deep RL agent is delicately designed and trained end-to-end to plan the 6-DOF movement of a US probe based on real-time US images, in order to autonomously navigate toward the standard views of the lumbar spine.
- We innovatively investigate the correlation between the navigation performance of the RL agent and the acoustic shadow characteristics in spinal sonography based on the US confidence map [16], and propose a novel view-specific acoustic shadow reward that utilizes the shadow information to implicitly guide the RL-based navigation.
- A location-sensitive DL agent is proposed to recognize the standard views of the lumbar spine from real-time US images, and jointly determines the movement of the probe with the RL agent through a dual-agent collaborative navigation workflow.
- A general approach is presented to build a simulation environment that models the probe-patient interaction in US imaging based on real-world US data, which can realize continuous state and action spaces for the development of US-guided navigation algorithms.

The remainder of this article is organized as follows: Section II provides an overview of the related work in the fields of US standard view detection and robotic US acquisitions. Then, we introduce the details of our presented method in Section III, before experiments and results are presented in Section IV. Conclusions and future perspectives are discussed in Section V.

II. Related Work

A. US Standard View Detection

As a leading machine learning tool in image analysis, DL has been intensively studied and applied to to the detection of standard views from 2D US image sequences [5] or 3D US volumes [17]. Some researchers detect the standard views from 3D US volumes by breaking down the 3D volume into 2D slices for image classification [17]. Lorenz et al. [18] used anatomical landmark detection to align the 3D volume with a model to localize the standard view planes. Other groups applied convolutional neural networks to regress the transformation from the current plane to the standard view plane in 3D US volumes [19]. However, this kind of prediction may cause abrupt changes in position, which may not be suitable for the robotic control of the US probe. Alansary et al. [20] customized an RL agent to learn the incremental adjustment of the plane parameters ($ax + by + cz + d = 0$) toward the standard views in MRI data, and Dou et al. [21] extended this method for standard view detection in 3D US data by performing landmark alignment and RL-based adjustment of the plane parameters. However, these methods focus on detecting the standard views from expert-acquired, pre-processed US images and have not taken the autonomous control of a robotic US probe into consideration. Instead, we are committed to directly establishing the relationship between the US image content and probe motion control with RL and DL techniques, in order to mimic the decision making process of expert sonographers to realize standard view acquisitions in robotic spinal sonography.

B. Robotic US acquisitions

A large number of robotic systems have been developed to automate the US imaging of different human tissues. The reader can refer to [13] for a literature review. Different methods have been proposed to plan the movement of the probe during robotic US acquisitions. In [22], the researchers transfer a manually planned scanning path in pre-operative MRI data to the actual patient during the intra-operative stage by registering the patient skin surface extracted from the MRI data to real-time RGB-D data. Other researchers directly plan the scanning path on the patient skin surface to cover a region of interest extracted from the RGB-D data [23]. Recently, an RL-based method is proposed to control 3 degrees of freedom (DOFs) of a US probe based on the observation of tissue surface by an RGB camera to realize US imaging of a soft target in the presence of occlusion and movement [24]. While these surface-based methods have demonstrated the feasibility to keep the probe in contact with the patient and acquire meaningful images, it may not always be feasible to identify the anatomy based on surface landmarks (e.g., in obese subjects) [25], which may reduce the versatility of these methods. Also, the US images that contain rich information of the anatomy have not been fully utilized in the probe motion planning.

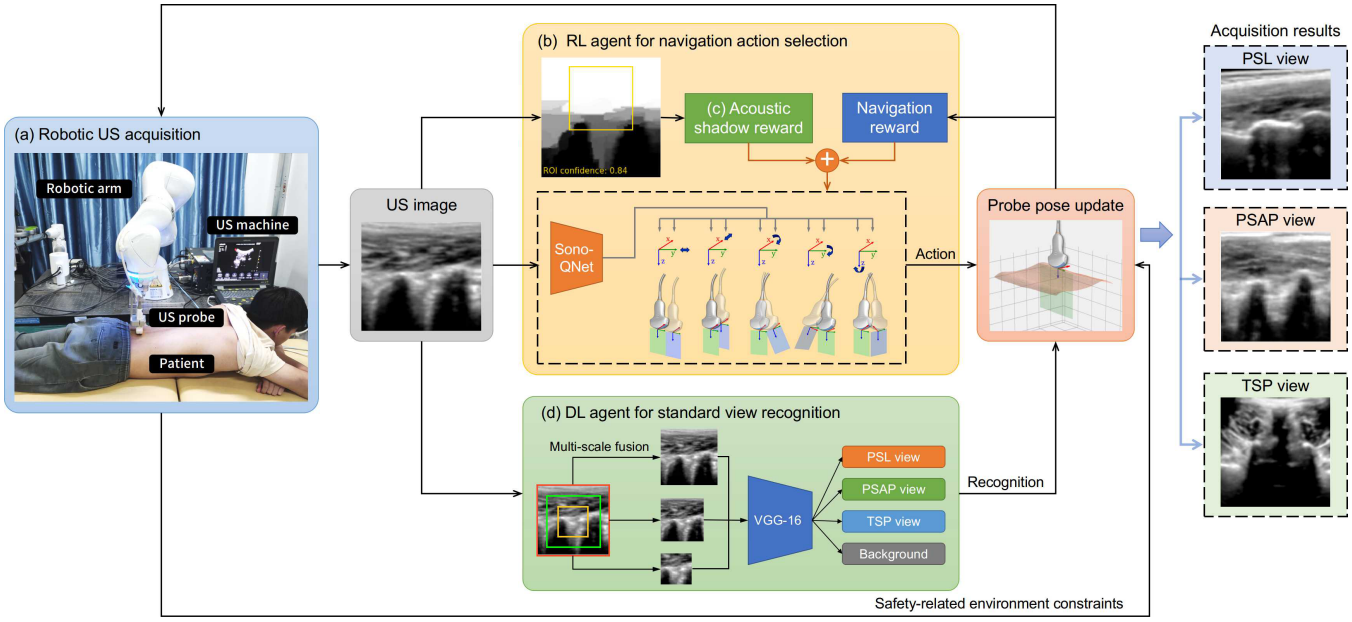

Fig. 2. Overview of the presented method for autonomous standard view acquisition in robotic spinal sonography. (a) shows the real-world system configuration, where a US probe is controlled by a robotic arm to scan the patient in the prone position. (b) Given the acquired US image as input, the RL agent selects the best navigation action based on the *SonoQNet* to control the 5-DOF movement of the probe. The US confidence map is computed from the US image to calculate the (c) view-specific acoustic shadow reward, which is used in combination with the navigation reward to train the RL agent. Meanwhile, (d) a pre-trained DL agent recognizes the standard views from the US image and jointly determines the movement of the probe under the safety-related environment constraints. The objective of the proposed framework is to automatically acquire three standard views of the lumbar spine (PSL, PSAP and TSP views).

Some researchers proposed US-based visual servoing methods [26], but they focus on stabilizing the view of an existing target in the image rather than automatically searching for an anatomy. In [27], an automatic scanning strategy is designed to search for the longitudinal plane of the carotid artery by detecting carotid landmarks using well-engineered features. In order to develop more generic methods, a number of machine learning-based solutions have been proposed to learn US probe guidance in a data-driven manner. Some researchers used imitation learning (IL) algorithms to learn 3-DOF guidance of the probe orientation from expert demonstrations in fetal US imaging [28]. However, the IL-based methods usually rely on complete and accurate demonstrations, which may be intractable or expensive to obtain [29]. Other groups applied RL to learn the navigation of a US probe based on self-generated experiences in simulation. Some researchers built the simulation environment with spatially tracked 2D US images acquired by a sonographer on a grid placed on the patient during cardiac [30] and spinal US imaging [31], and used RL to learn probe control with 2 to 4 DOFs. However, these methods have limited state-action spaces due to the design of simulation environments, which would reduce the flexibility of the RL agent. In [32], we preliminarily developed a deep RL solution to the 6-DOF control of the probe in a simulation environment built with reconstructed 3D volumes that cover the anatomy of interest, which can improve the flexibility of the learned navigation policy.

A distinction between our work and the above works is that we explicitly focus on a system that enables fully automatic 6-DOF control of the US probe based on real-time US images to search for multiple standard views in spinal sonography. Therefore, the system does not rely on manual planning of the scanning path, preoperative tomographic imaging, surface landmark detection or manual initialization of the probe position. Also, our method does not require expert demonstration data, and is not restricted by limited state-action pairs. Instead, we build a simulation environment for probe-patient interaction using real-world US data, and propose a framework based on RL and DL to automatically interpret US images and autonomously plan the movement of the probe.

III. Methodology

A. Simulation of Probe-Patient Interaction

Since the RL agent learns the optimal policy through trial and error, it is unsafe and impractical to directly train the US probe navigation agent on real patients. A feasible solution is to build a simulation environment with real-world data to train the RL agent. Different from previous studies [30][31] that build the simulation environment with manually acquired, spatially tracked 2D US frames, we build the simulation environment with reconstructed 3D volumes of the lumbar spine acquired in real-world US scans. Since we use a reconstructed volume as the virtual patient in our simulation, any slice with arbitrary position and orientation can be sampled in the volume, which can significantly enlarge the state-action spaces for more realistic simulation of probe-patient interaction.

In order to acquire US data from real volunteers, we built a robotic system as shown in Fig. 2(a). The system used a robotic arm (KUKA LBR iiwa 7 R800, KUKA Roboter GmbH, Germany) to control the movement of a convex US probe (C5-1B, Shenzhen Wisonic Medical Technology Co., Ltd, China) attached to its end-effector. We asked the volunteers to lie in the prone position on a horizontal bed, and a

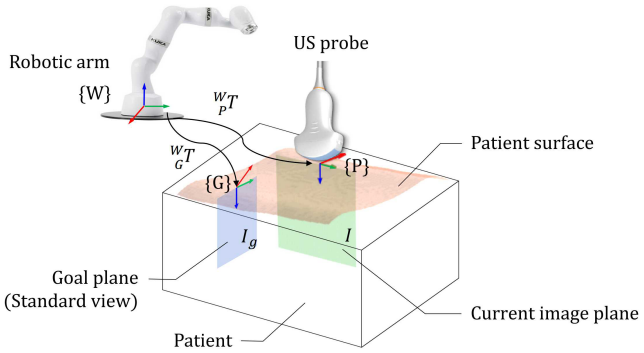

Fig. 3. Illustration of the simulation environment for robotic spinal sonography. The virtual patients in our simulation are reconstructed 3D volumes of the lumbar spine, and the virtual probe is modeled as a commonly used 2D probe with a square field-of-view. The imaging plane of the probe is set as the y-z plane of the probe frame $\{P\}$. The world frame $\{W\}$ is attached to the robot base. The current probe pose and the goal probe pose associated with the target standard view are represented by the transformations ${}^{W}_{P}\mathbf{T}$ and ${}^{W}_{G}\mathbf{T}$, and the corresponding US images are denoted by I and I_g, respectively.

clinician manually configured the US imaging parameters and spread the coupling gel over the skin surface of the volunteers. The start and end points of the scan were specified by the clinician to cover the lumbar spine, and the robot linearly moved the US probe under Cartesian impedance control while applying a downward force of $5N$ to ensure acoustic couping. We set a high stiffness ($2000N/m$) in the horizontal directions and a low stiffness ($50N/m$) in the vertical direction for compliance. The acquired B-mode images and the corresponding probe poses estimated based on the robotic arm kinematics and US hand-eye calibration [33] were recorded for volume reconstruction with a squared distance weighted approach [34]. Three sweeps were performed on each volunteer. Finally, the reconstructed volumes were manually screened to remove the data with poor quality, yielding a total of 41 US volumes of 17 healthy male volunteers aged 23 ± 3 years old. The average volume size of our dataset is $350 \times 397 \times 274$ and the size of each voxel is $0.5 \times 0.5 \times 0.5mm^3$. After each robotic acquisition, the clinician manually acquired three standard views of the lumbar spine on each volunteer and the corresponding probe poses were recorded.

An overview of our simulation environment is shown in Fig. 3. The transformation from the world frame (robot base) $\{W\}$ to the probe frame $\{P\}$ is denoted as ${}^{W}_{P}\mathbf{T}$, which is a 4×4 matrix that describes the current 6-DOF pose of the probe. The goal probe pose $\{G\}$ associated with the target standard view is described as transformation ${}^{W}_{G}\mathbf{T}$. Without loss of generality, we assume the virtual probe in our simulation as a commonly used 2D probe with a field-of-view of 150×150 pixels, and the imaging plane is defined as the y-z plane of the probe frame $\{P\}$. Given a virtual patient (US volume) and an arbitrary probe pose ${}^{W}_{P}\mathbf{T}$, the acquired US image I can be uniquely determined by sampling in the volume. In our simulation environment, the skin surface of each virtual patient is extracted as $z = f(x, y)$ based on the intensity of the 3D US volume. In real-world applications, the patient skin surface can be extracted using external sensor data, such as RGB-D or lidar information [22].

The ground truth B-mode images of the three standard views acquired by the clinician and the corresponding images acquired by the virtual probe with the recorded poses in our simulation are compared in Fig. 1(b). It can be seen that in spite of a slight deterioration in resolution, the images acquired from the virtual patient can preserve important anatomical structures in the B-mode images, which shows that our simulation environment can realistically reproduce the real-world US acquisitions.

B. Reinforcement Learning for Navigation Action Selection

1) Problem formulation: In the RL framework, an agent learns the behavior policy by interacting with the environment through a sequence of states, actions and rewards. Here, we formulate the task of the US acquisition robot to observe US images and navigate the probe toward a target standard view as a partially observed sequential decision making problem in the RL framework.

a) States and observations: The full state of the probe-holding agent can be represented as $({}^{W}_{P}\mathbf{T}, {}^{W}_{G}\mathbf{T}, I, I_g)$, indicating the current and goal probe poses and the corresponding US images, as described in Section III-A. We assume that the patient anatomy and the relative pose between the robot and the patient are unknown. Therefore, the goal probe pose and image are unobservable to the agent, and the agent can only observe the acquired US image I and make navigation decisions. In order to take advantage of the dynamic information, we use a sequence of 4 recently acquired images as the observation at time t: $s_t = [I_{t-3}, \cdots, I_t]$.

b) Navigation actions: The policy of the RL agent $\pi\colon s_t \mapsto a_t$ maps from the current observation s_t to a navigation action a_t. In order to make the learned actions more versatile and independent of the actual patient position and orientation, different from previous methods that represent the actions in the world frame [30][31], we follow a probe-centric parameterization and define the navigation action a as a transformation operator ${}^{P}\mathbf{T}$ with respect to the probe frame $\{P\}$, so that the probe is moved by

$$ {}^{W}_{P}\mathbf{T} \leftarrow {}^{W}_{P}\mathbf{T} \cdot {}^{P}\mathbf{T} \tag{1} $$

Since ${}^{P}\mathbf{T}$ contains 16 parameters under constraints to represent a valid transformation, directly learning these parameters will be intractable and the interpretability of the learned policy will be limited. Also, a small change of the parameters may result in an abrupt change of the probe pose, which is not favorable in the US probe navigation task. To address these issues, we discretize the action space into 10 action primitives associated with 5 DOFs of the probe, as shown in Fig. 2 (b). Four actions represent the translation of the probe along $\pm x$, $\pm y$ axes of the probe, and six actions represent the rotation around $\pm x$, $\pm y$, $\pm z$ axes of the probe. We adopt hierarchical action steps to navigate the probe in a coarse-to-fine manner, similar to [32]. Specifically, the action step d_{step} and θ_{step} are initialized as $5mm/5°$. 30 most recent probe poses are stored in a buffer with the format of $(\boldsymbol{p}_t, \boldsymbol{q}_t)$, where $\boldsymbol{p}_t$ is the position of the probe at time t and $\boldsymbol{q}_t$ is the quaternion representation

of the probe orientation. If at least 3 pairs among the 30 most recent probe poses have a pairwise Euclidean distance smaller than 0.01, the probe pose is assumed to have converged and the action step will be decreased by $1mm/1^\circ$.

c) State transition under constraints: Different from previous work that directly apply the navigation action selected by the agent [30][31], we take into account some safety-related environment constraints in real-world US scans to update the probe pose, as shown in Fig. 2. First, we consider the practical requirement that the probe be placed over the skin surface to ensure good acoustic coupling. Since the virtual patient in our simulation is roughly parallel with the horizontal plane (see Section III-A), we use 1-DOF translational movement of the probe in the $\pm z$ direction to follow the patient surface $z = f(x, y)$. Second, to ensure good probe-patient contact and guarantee patient safety, the tilt angle of the probe (angle between the imaging plane and the vertical direction) should be limited. Therefore, after the new probe orientation is calculated, the tilt angle is calculated as

$$\alpha = \arccos(\hat{\boldsymbol{z}}_p, [0, 0, -1]^T) = \arccos[-{}^W_P\mathbf{T}(3, 3)] \tag{2}$$

where $\hat{\boldsymbol{z}}_p$ is a unit vector along the z-axis of the probe. We limit the tilt angle to be smaller than 30°. If $\alpha > 30^\circ$, the probe orientation will not be updated.

After the new probe pose is determined under the above constraints, a new US image can be acquired from the virtual patient, and the state of the probe will be updated.

d) Reward function: In our task, the reward function used for RL training should encourage the agent to minimize the distance to goal, which can be represented by

$$d_t = \left\|\boldsymbol{p}_t - \boldsymbol{p}_g\right\|_2, \ \theta_t = 2\arccos(|\langle \boldsymbol{q}_t, \boldsymbol{q}_g \rangle|) \tag{3}$$

where $\|\cdot\|_2$ is the L2 norm and $\langle \cdot, \cdot \rangle$ is the inner product. By definition, d_t measures the Euclidean distance between the current probe position and the goal position at time t, and θ_t is the minimum angle required to rotate from the current probe orientation to the goal orientation.

Some methods construct a dense reward function by classifying the actions as "good" (moving closer to the goal) or "bad" (moving away from the goal), and assigning rewards with manually set values [30][31]. Similar to [32], we design the navigation reward at time t to be proportional to the amount of pose improvement normalized by the action steps

$$\begin{aligned} r_{nav,t} &= \Delta d_t + \Delta\theta_t, \\ \text{where} \quad \Delta d_t &= \frac{d_{t-1} - d_t}{d_{step}} \in [-1, 1], \\ \Delta\theta_t &= \frac{\theta_{t-1} - \theta_t}{\theta_{step}} \in [-1, 1] \end{aligned} \tag{4}$$

Note that $r_{nav,t} \in [-1, 1]$ since the action in each step is either translation or rotation. In addition, we assign a high reward ($+10$) for task accomplishment ($d_t \leq 1mm$ and $\theta_t \leq 1^\circ$) and add some penalties based on the safety-related constraints. When the tilt angle of the probe α exceeds 30°, the agent will receive a penalty of -0.5. When the probe moves outside the patient volume (the proportion of pixels with non-zero gray value in I_t is less than 30%), the agent will get a reward of -1. In summary, the reward at time step t is defined as

$$r_t = \begin{cases} -1, & \text{if moving out of patient;} \\ -0.5, & \text{if } \alpha > 30^\circ; \\ 10, & \text{if reaching goal;} \\ r_{nav,t}, & \text{otherwise.} \end{cases} \tag{5}$$

e) Termination conditions: During training, we define four conditions to terminate the navigation: (i) the goal is reached; (ii) the number of steps exceeds the maximum limit (e.g., 120); (iii) the action step is decreased to zero; and (iv) the probe moves out of the patient. Only the last three conditions are used during inference, since the true location of the standard plane is assumed unknown to the agent.

2) Deep reinforcement learning algorithm: The learning goal of the RL agent is to maximize the return or discounted cumulative future rewards

$$G_t = r_{t+1} + \gamma r_{t+2} + \gamma^2 r_{t+3} + \cdots + \gamma^{T-t-1} r_T \tag{6}$$

where $\gamma \in (0, 1)$ is a discount factor and T is the time step when the episode is terminated. The state-action value function $Q^\pi(s, a)$ is defined as the expected return following policy π: $Q^\pi(s, a) = \mathbb{E}_\pi[G_t | s_t = s, a_t = a]$. The optimal Q-function $Q^*(s, a) = \max_\pi Q^\pi(s, a)$ following any policy π is known to satisfy the Bellman equation

$$Q^*(s, a) = \mathbb{E}_{s'}[r(s, a) + \gamma \max_{a'} Q^*(s', a')] \tag{7}$$

If $Q^*(s, a)$ is known, then the optimal policy can be determined by $\pi^* = \arg\max_a Q^*(s, a)$. In this work, we use a deep neural network $Q(s, a; w)$ to approximate $Q^*(s, a)$, and train the network with the deep Q-learning algorithm [35]. The deep Q-network architecture used in our method is referred to as *SonoQNet*, as illustrated in Fig. 4. It is modified from the SonoNet-16 architecture [5], which was originally proposed for real-time detection of standard views in fetal US images. The input of SonoQNet are 4 recently acquired US images, and the output are the approximated Q-values for the 10 navigation actions. The optimal network parameters w^* can be learned

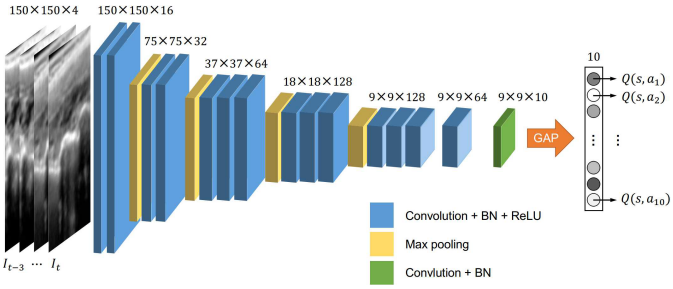

Fig. 4. Schematic illustration of the SonoQNet architecture for navigation action selection. The input are 4 recently acquired US images of size 150×150. The output are the predicted Q-values for the 10 navigation actions, and the agent will select the action with the highest Q-value. The feature extractor contains 13 convolutional layers (blue), each followed by batch normalization and ReLU activation. Max pooling (yellow) is performed after the first 4 convolutional blocks with a filter size of 2×2 and a stride of 2. The size of each feature map is denoted above the blocks. The output of the last convolution+BN block (green) are 10 class score maps associated with the 10 navigation actions, which are finally aggregated by global average pooling (GAP) to approximate the Q-values.

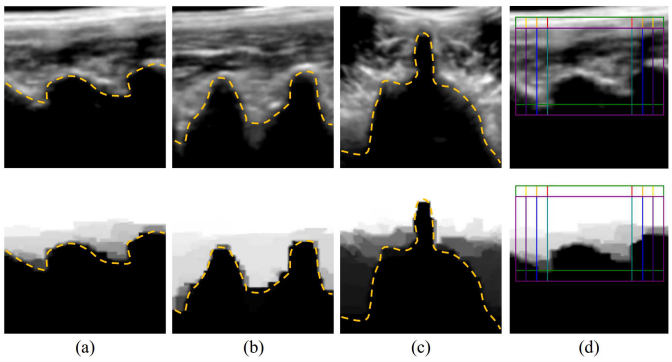

Fig. 5. (a)-(c) show the US images and the corresponding confidence maps of the PSL view, PSAP view and TSP view of the spine. The acoustic shadow can be seen in the images as area below the yellow dotted line. (d) illustrates the proposed ROI candidates to quantitatively measure the shadow area.

by iteratively updating w with stochastic gradient descent to minimize the loss function

$$L(w_i) = \mathbb{E}_{s,a,r,s'}[(r + \gamma \max_{a'} Q(s', a'; w_{i-1}) - Q(s, a; w_i))^2] \tag{8}$$

where w_i is the weight in the i-th iteration.

3) Implementation details: The SonoQNet is trained by the temporal-difference method with experience replay and target network techniques described in [35]. In our implementation, we train the network every 10 interaction steps with a batch size of 32 using Adam optimizer [36], and the target nerwork is updated every $1k$ training steps. The discount factor γ is 0.9. The capacity of experience replay memory is $100k$. During initialization, the network is updated for $10k$ iterations with a learning rate of 0.01 on experiences generated by a supervised policy, which selects the actions to minimize the distance-to-goal. Subsequently, the network is trained for $200k$ iterations on self-generated experiences with an ε-greedy policy. The exploration rate ε linearly decays from 0.5 to 0.1 in the first $100k$ interactions steps and remains unchanged thereafter. The learning rate is set to 0.01 for the first $40k$ training steps, 0.001 for the next $40k$ steps, 5e-4 for the next $30k$ steps, and 1e-4 for the remaining steps.

C. View-specific Acoustic Shadow Reward

1) Acoustic shadow estimation with US confidence map: Due to the nature of sound propagation, the US signal will be strongly attenuated at the tissue-bone interface, resulting in acoustic shadows after the interface. In most cases, the shadowing artifacts in US images should be avoided to improve the imaging quality. In spinal sonography, however, the shadows can produce some sonographic patterns that can help locate the spine anatomy [7]. For instance, the shadow patterns in the PSL and PSAP views are referred to as the "horse head sign" and the "camel hump sign", and the acoustic shadow in the TSP view appears as a tall dense acoustic shadow, as shown in Fig. 5(a-c). Therefore, we speculate that additionally taking into account the shadow information may improve the navigation performance in spinal sonography.

In this work, we detect the shadow regions from the US image I_t by calculating its US confidence map at time step t, $C_t \leftarrow confidenceMap(I_t)$, $C_t(i,j) \in [0,1]$, based on the method in [16] that estimates the per-pixel confidence in the US image to emphasize the uncertainty in shadow regions using a random walks framework. A lower confidence value of a pixel indicates an increased likelihood of acoustic shadow. As shown in Fig. 5(a)-(c), the possible shadowed regions in the US images are highlighted in the confidence maps. Moreover, based on the insight that different standard view acquisition tasks may require different underlying shadow patterns, we calculate the average confidence in a view-specific region of interest (ROI) in the image:

$$c_t = \frac{1}{|S|} \sum_{(i,j) \in S} C_t(i,j) \tag{9}$$

where S denotes the selected ROI for the target standard view. Note that the shadow density in S can be represented by $1 - c_t$. The confidence change in the ROI at time step t can be represented by $\Delta c_t = c_t - c_{t-1} \in [-1, 1]$.

A total of 8 ROI candidates are proposed, as shown in Fig. 5(d). They are selected as rectangles centered horizontally in the image and offset 10 or 20 pixels from the top edge. The height of the ROI is set as 80 and the width is chosen from $\{80, 100, 120, 140\}$. The selection of these band-like regions is based on the observation that the top region (with a height of about 10 pixels) is almost completely located above the tissue-bone interface, and the bottom region (with a height of 50 pixels) is almost completely located below the tissue-bone interface, which can hardly provide any discriminating shadow information.

2) Selection of view-specific region of interest: In order to select view-specific ROIs for different tasks, we analyze the relationship between the navigation performance of the RL agent and the shadow characteristics in each task. As shown in Fig. 6(a-c), the average navigation reward per step R_{nav}, final position error d, and final orientation error θ against the average confidence change per step Δc of the RL agent during training in the PSL, PSAP and TSP view acquisitions are illustrated. It can be seen in Fig. 6(a-b) no matter which ROI configuration is used, as Δc increases, the pose improvement becomes greater and the final pose error becomes smaller. This indicates that the navigation performance toward the PSL and PSAP views are positively correlated with an improved confidence in the ROI, and the agent implicitly learns to reduce the shadow area in the ROI during learning of the navigation policy. This is probably because most of the shadow region appears below the ROI in these standard views (see Fig. 5(a-b)). Differently, for the navigation toward the TSP view, a negative correlation between the navigation performance and the confidence change is observed, which implies that the agent learns to maximize the shadow region during the search for the TSP view, which may be due to the tall dense acoustic shadow in the image center under the spinous process (see Fig. 5(c)). To find the ROI configuration that is most related to the navigation performance in each task, we use Pearson's correlation coefficient (PCC) to quantitatively measure the relationship between the navigation performance and the confidence improvement of different ROIs. PCC measures the

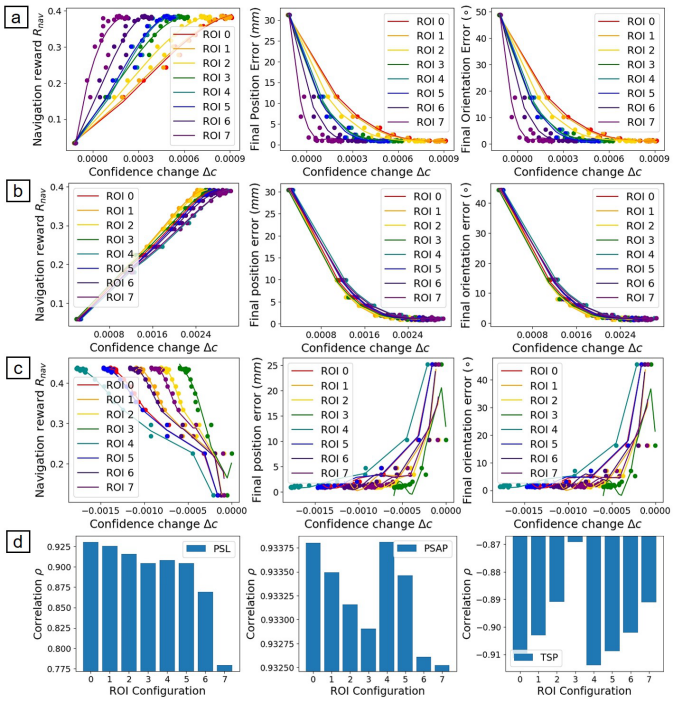

Fig. 6. (a-c) show the average navigation reward per step R_{nav}, final position error d, and final orientation error θ against the average ROI confidence change per step Δc during RL training to acquire the PSL, PSAP and TSP views, respectively. The results using different ROI configurations are indicated by different colors. (d) shows the correlation ρ that measures the relationship between the navigation performance and the confidence change in different ROIs during the acquisition of the three standard views.

linear relationship between two variables X and Y, which can be calculated by

$$\rho(X,Y) = \frac{\mathbb{E}[(X-\mu_X)(Y-\mu_Y)]}{\sigma_X \sigma_Y} \tag{10}$$

where μ_X, μ_Y are the means of X and Y, respectively, and σ_X, σ_Y are standard deviations of X and Y. $\rho(X,Y) \in [-1,+1]$. In order to take into account both the navigation efficiency and accuracy, we calculate a weighted combination of the PCCs between R_{nav}, d, θ and Δc:

$$\rho = \alpha_1 \rho(R_{nav}, \Delta c) + \alpha_2 \rho(-d, \Delta c) + \alpha_3 \rho(-\theta, \Delta c) \tag{11}$$

where the weights are empirically set as $\alpha_1 = 0.5$, $\alpha_2 = \alpha_3 = 0.25$. Therefore, $\rho \in [-1,+1]$ indicates the correlation between the overall navigation performance and confidence change in the training data.

The correlation ρ of different ROI configurations in different tasks are shown in Fig. 6(d). It can be seen that the navigation performance toward the PSL view is most strongly correlated with the confidence improvement in ROI No. 0 , which is a small square region of size 80×80, offset 10 from the top edge. For the acquisition of PSAP view, ROI No. 1 is selected (size 80×80, offset 20 from the top edge). This may be because the tissue-bone interface is deeper in the PSAP view than in the PSL view. For the TSP view acquisition, ROI No. 1 has the largest negative correlation with the navigation performance, which implies that the agent intends to maximize the shadow area in this region.

3) Hybrid reward function: In order to utilize the shadow information to guide the navigation, we introduce a view-specific acoustic shadow reward (ASR) $r_{as,t} = \Delta c_t = c_t - c_{t-1}$ in the original reward function (5) for RL training:

$$r_t = \begin{cases} -1, & \text{if moving out of patient;} \\ -0.5, & \text{if } \alpha > 30°; \\ 10, & \text{if reaching goal;} \\ r_{nav,t} + \lambda r_{sa,t}, & \text{otherwise.} \end{cases} \tag{12}$$

where $\lambda = 1$ is used in the acquisition of PSL and PSAP views to encourage confidence improvement in the ROI and $\lambda = -1$ is used for the TSP view to encourage shadow area maximization in the ROI.

D. Deep Learning for Standard View Recognition

Although the RL agent can decide the step-by-step movement of the US probe based on the US images, the navigation is "blindly" terminated, i.e., the navigation is stopped after the probe pose gradually converges, and the finally acquired image is assumed the best. This strategy may bring some problems. For example, the RL agent may be trapped at a location and the navigation will be quickly terminated without further exploration. Another case is that the agent may have acquired the standard view, but mistakenly moves away to a suboptimal position. To this end, a method should be proposed to enable active termination and exploration of the RL agent. Some methods determines the best stopping position of the RL agent based on the Q-values [20][21], but these methods may not have a good interpretability. Therefore, we propose to use a pre-trained DL agent to recognize the standard views from the US images to provide feedback to the RL agent and jointly determine the movement of the probe.

1) Deep neural network fine-tuning: In this work, we adopt the VGG-16 [37], one of the state-of-the-art architectures for image classification, as the basic deep neural network model for our standard view recognition task. We initialize the network with publicly available weights trained on the ImageNet dataset [38]. Then, the original top fully connected layer is replaced with a fully connected layer with 4 outputs corresponding to the 3 standard views and background, and initialized with random weights. The network is fine-tuned on our training data (US images with class labels associated with the three standard views and background) using stochastic gradient descent and cross-entropy loss with a batch size of 16 for 50 epochs to achieve stable performance. A small learning rate of 0.0001 is used in training.

2) Multi-scale fusion: In our task, the spatial location of pixels in the US image plays an important role to correctly locate the spine anatomy for standard view recognition. To this end, we propose a multi-scale fusion (MSF) approach to make the classification network more sensitive to location features. Instead of using the whole image as input of the network, we accumulate multiple scales of the US image (100%, 75% and 50% around the image center) as different channels, as shown in Fig. 2(d). Note that this approach will not increase the overall complexity of the network.

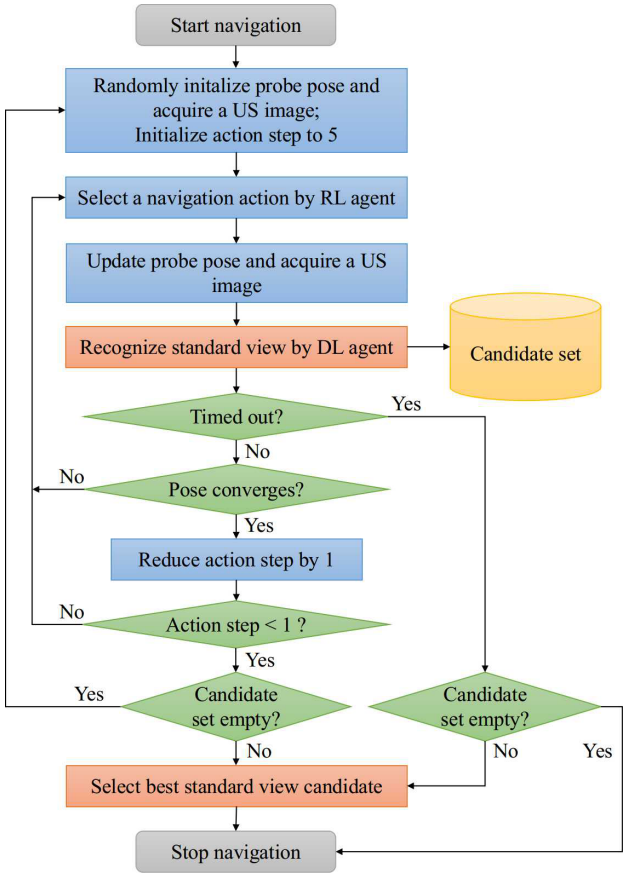

Fig. 7. Workflow of the dual-agent collaborative navigation method for standard view acquisition. The blue boxes indicate the operations by the RL agent and the orange boxes indicate the operations by the DL agent. The standard view recognition results of the DL agent are used as feedback to enable active termination and exploration of the RL agent.

E. Workflow of Dual-agent Collaborative Navigation

In order to integrate the RL and DL agents to improve the acquisition results, we propose a workflow to allow collaboration of the two agents to jointly determine the movement of the US probe, as shown in Fig. 7. Each time the RL agent selects a navigation action and acquires an image, the DL agent will detect and save possible standard view images with a predicted probability over 0.5 in a candidate set. After the RL action step is reduced to zero or time is out, the candidate set will be inspected. If it is not empty, the last recorded standard view candidate during RL navigation will be selected as the best stopping position. We use the last recorded candidate rather than the candidate with the highest predicted probability because i) the standard view recognition result may not be accurate, and ii) it is likely that a position at a later stage in the RL navigation trajectory is more reliable than one in an earlier stage. If time is out but the candidate set is empty, the navigation will be directly terminated. If no standard view is detected during RL navigation and there is still time left, the probe will be randomly repositioned on the patient, and the previous navigation process will be repeated until the total number of steps exceeds the limit.

TABLE I
CLASSIFICATION SCORES OF DIFFERENT MODELS

Model	Precision	Recall	F1-score
VGG-16	0.9281	0.9249	0.9233
VGG-16 + MSF	**0.9603**	**0.9594**	**0.9589**

IV. EXPERIMENTS

A. Dataset

Among the whole dataset of 41 US volumes acquired from 17 subjects using the pipeline described in Section III-A, 25 US volumes of 14 subjects are used for training of the RL agent, and the remaining data is split into two testing datasets associated with two different settings, i.e., *intra-subject* and *inter-subject*, in order to fully evaluate the effectiveness of the proposed methods. In the *intra-subject* setting, the agent is evaluated on 8 unseen data volumes acquired from 8 seen subjects over time. This setting is designed to evaluate the effectiveness of the method to perform reproducible US acquisitions on familiar subjects in the presence of target displacement and tissue deformation; this is important in the medical applications that require multiple US acquisitions of the same patient, such as pre- and post-operative ultrasonography. The *inter-subject* setting is more challenging, which requires the agent to be evaluated on 8 data volumes acquired from 3 unseen subjects. This task is more difficult as it requires the learned policy to be generalized to out-of-distribution data and deal with highly variable patient anatomy.

B. Evaluation of the Standard View Recognition Module

In order to train and test the DL agent for standard view recognition, we create a training set and a testing set by sampling in the 25 training data volumes and 8 testing data volumes in the inter-subject setting. Specifically, the position of the probe is sampled with a 10-pixel interval within 40% around the center of the volume to avoid sampling outside the patient. The orientation of the probe is sampled densely around the standard view orientations by rotating around the z-axis by -10° to 10° with an interval of 2°, and sampled sparsely in other orientations by rotating around the z-axis by 30° to 360° with an interval of 30°. The sampled image is annotated as a standard view image if the probe pose is within $10mm$ and 10° from a standard view pose and the structural similarity (SSIM) between the acquired image and the ground-truth standard view image is larger than 0.5, and annotated as background if the corresponding probe pose is more than $20mm/20^\circ$ away from all standard views. Finally, a total of 1956 images (PSL: 535, PSAP: 381, TSP: 648, BG: 392) and 493 images (PSL: 118, PSAP: 155, TSP: 100, BG: 120) are collected for training and testing purposes, respectively.

We quantitatively evaluate the classification performance of the DL agent for standard view recognition on the test data using the precision, recall and F1-score. The results of the fine-tuned VGG-16 models with and without using the MSF approach are reported in Table I. Moreover, the confusion matrices on the test data are shown in Fig. 8 for a clear

TABLE II
PERFORMANCE EVALUATION OF DIFFERENT METHODS FOR STANDARD VIEW ACQUISITION

Test setting	Method	Final position error (mm)				Final orientation error ($^\circ$)				SSIM			
		PSL view	PSAP view	TSP view	Average	PSL view	PSAP view	TSP view	Average	PSL view	PSAP view	TSP view	Average
Intra-subject	RL	9.55±11.96	9.06±15.76	8.78±8.35	9.13±12.40	7.27±13.53	17.31±43.38	6.73±2.81	10.44±26.29	0.49±0.18	0.46±0.16	0.51±0.22	0.49±0.33
	RL + ASR	5.73±4.89	7.94±9.53	7.14±10.18	6.94±8.53	6.74±10.92	9.57±22.98	**6.19±3.77**	7.50±14.85	0.57±0.20	0.44±0.16	0.56±0.20	0.52±0.32
	RL + DL	6.14±6.41	6.64±11.48	7.18±6.30	6.65±8.42	4.81±3.56	10.02±28.07	6.50±2.99	7.11±16.43	0.57±0.15	0.48±0.14	0.53±0.22	0.53±0.30
	RL + ASR + DL	**3.76±3.42**	**4.78±2.02**	**7.01±9.30**	**5.18±5.84**	**4.66±4.22**	**4.51±2.98**	6.57±4.34	**5.25±3.90**	**0.66±0.14**	**0.48±0.12**	**0.58±0.18**	**0.57±0.26**
Inter-subject	RL	24.97±20.69	14.05±12.32	16.41±24.63	18.48±19.89	39.96±55.43	29.21±47.56	19.28±30.24	29.48±45.64	0.30±0.09	0.33±0.10	0.46±0.15	0.36±0.20
	RL + ASR	18.51±16.37	14.38±16.26	11.71±22.27	14.87±18.51	**15.32±26.08**	24.67±46.34	10.93±13.61	**16.97±31.69**	0.33±0.10	0.33±0.08	0.45±0.16	0.37±0.20
	RL + DL	26.21±23.02	11.16±9.94	11.07±8.85	16.15±15.35	27.65±37.78	**19.75±45.93**	**7.20±4.24**	18.20±34.42	0.39±0.12	**0.37±0.10**	0.49±0.15	0.42±0.22
	RL + ASR + DL	**18.07±11.35**	**10.96±11.99**	**9.57±10.00**	**12.87±11.14**	18.39±31.16	19.96±43.29	14.13±30.95	17.49±35.60	**0.43±0.09**	0.35±0.07	**0.49±0.14**	**0.43±0.18**

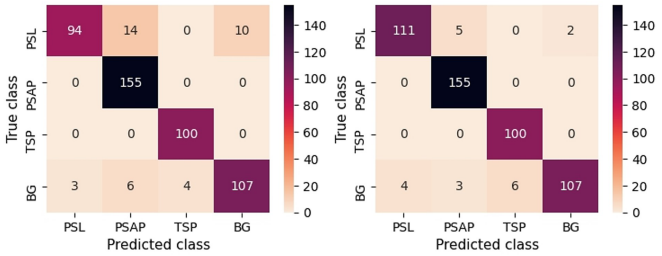

(a) (b)

Fig. 8. Confusion matrices of the (a) VGG-16 and (b) VGG-16+MSF models for standard view recognition on the test images.

comparison. It can be observed that the proposed MSF approach can effectively improve the classification performance of the network without increasing the complexity and number of parameters. As shown in Fig. 8, all the PSAP and TSP views are classified accurately by both models, while the VGG-16+MSF model can recognize the PSL views with a higher accuracy, showing that our localization sensitive approach can yield better classification performance.

C. Evaluation of the Overall Framework for Standard View Acquisitions

Then, we conduct both quantitative and qualitative experiments to evaluate the overall performance of our proposed framework for standard view acquisitions. Ablation studies are performed to validate the effectiveness of the three components in our proposed framework: the basic RL agent, the view-specific acoustic shadow reward (ASR), and the dual-agent collaborative navigation. Each of the four variations of our method (i.e., "RL", "RL+ASR", "RL+DL", "RL+ASR+DL") is evaluated on 24 random test cases (including 3 navigation tests on each test data) toward each of the three standard views in both the intra- and inter-subject settings. In each navigation episode during the training and testing of the RL agent, the pose of the probe is randomly initialized as follows. The horizontal position of the probe is randomly sampled in the center region $\{(x, y) : x \sim \mathcal{U}(0.3W, 0.7W), y \sim \mathcal{U}(0.2L, 0.8L)\}$ of patient data to avoid sampling outside the patient, where L, W are the length and width of the US volume, and the height of the probe is then adapted to the patient surface. The z-axis of the probe is initialized to be aligned with the $-z$ direction of the world frame, and the probe is randomly rotated around its z-axis by $\eta \sim \mathcal{U}(0, 360^\circ)\}$. The maximum number of steps in each episode is limited to 120. We use the final position error, final orientation error and structural similarity (SSIM) between the acquired image and the target standard view image as the evaluation metrics, to consider the navigation accuracy in terms of both the actual distance and the image content. The results are reported in Table II.

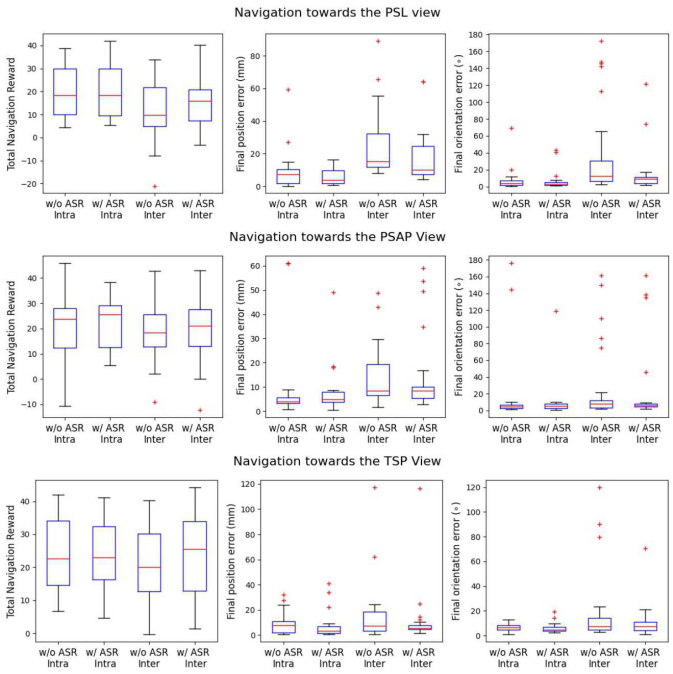

Fig. 9. Navigation performance of the RL agent with and without using the view-specific acoustic shadow reward (ASR) toward the PSL view (first line), PSAP view (second line) and TSP view (third line). The box-plots illustrate the evaluation metrics (total navigation reward, final position error and final orientation error) for every test case. In each box-plot, the first two columns show the performance of the methods in the intra-subject setting, and the last two columns show the performance of the methods in the inter-subject setting.

1) Evaluation of view-specific acoustic shadow reward: We first evaluate the RL agents trained with and without using ASR (i.e., by applying the reward function in (12) or (5)), and compare their navigation performance in the acquisition of the three standard views of the spine. We also compare the cumulative navigation reward $\sum_{t=0}^{T} r_{nav,t}$ and final pose error of the two agents in both test settings in Fig. 9. As shown in Table II (lines 1-2, 5-6), the navigation accuracy of the "RL+ASR" agent in both position and orientation shows a remarkable improvement of $2.19mm/2.94^\circ$ and $3.61mm/12.51^\circ$ over the "RL" agent in the intra- and inter-subject settings, respectively, and the SSIM is also improved by 3% and 1% in the two settings. It can be observed in Fig. 9 that by applying ASR in

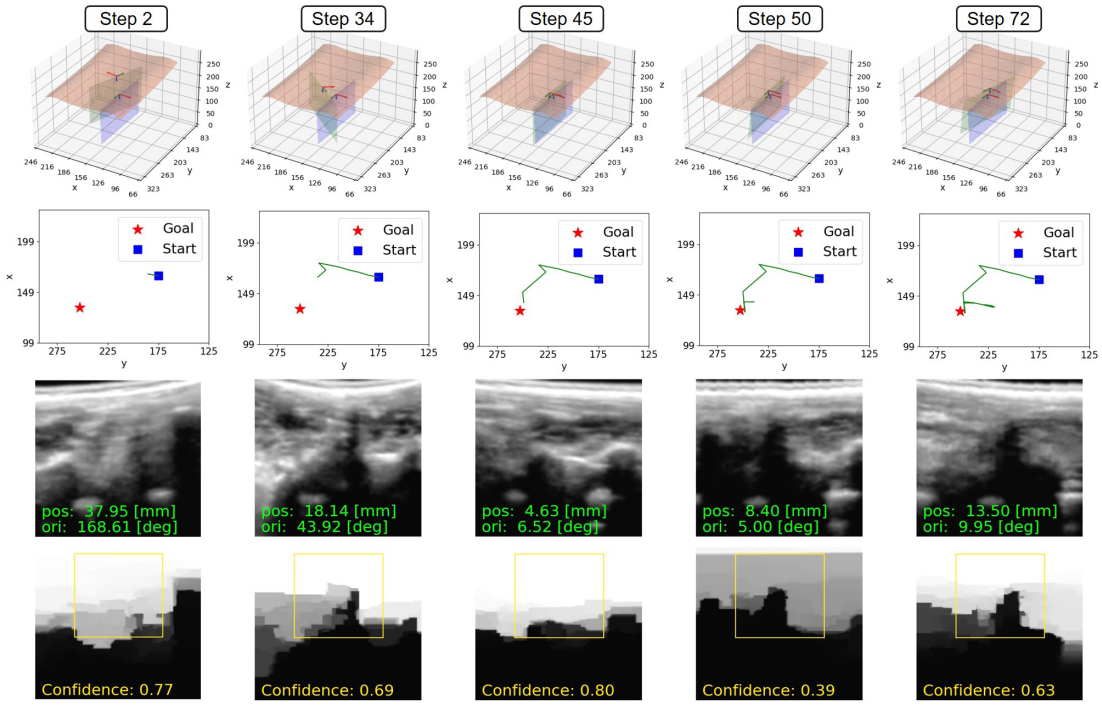

Fig. 10. Navigation trajectory of the "RL" agent toward the PSL view in an example test case. The first line shows the 3D plots of the virtual patient surface (salmon), current imaging plane (green), goal plane (blue), and the corresponding probe poses. The second line shows the top-view trajectory of the agent on the horizontal plane (green lines). The start and goal positions are indicated by a blue square and a red star, respectively. The US images are shown in the third line, with the pose errors marked in green. The confidence maps are plotted at the bottom, with the average confidence value of the selected ROI (yellow rectangle) marked in yellow.

the RL training, the cumulative navigation rewards are slightly increased, and the final position and orientation errors are generally lower compared with the basic RL agent trained without using ASR, especially in the more challenging inter-subject setting.

We also compare the navigation performance of the "RL+DL" and "RL+ASR+DL" methods to see the effectiveness of the ASR module when using RL-DL collaborative navigation to determine the probe movement. As shown in Table II (lines 3-4, 7-8), the "RL+ASR+DL" method yields a better navigation performance over "RL+DL", with a final pose error of $5.18mm/5.25°$ and $12.87mm/17.49°$ in the intra- and inter-subject settings, respectively, and the SSIM is increased by 4% and 1% in the two settings. The results show that the use of acoustic shadow information in our method can implicitly improve the navigation performance of the RL agent, which is consistent with the prediction in Section III-C. It should also be noted that a decline in the orientation accuracy by the "RL+ASR+DL" method toward the TSP view is witnessed, which may be due to the inaccuracy introduced by the DL-based standard view recognition module.

For a qualitative evaluation, we illustrate the navigation trajectories by the "RL" and "RL+ASR" agents toward the PSL view in an example test case in Fig. 10 and Fig. 11, respectively. As shown in Fig. 10 and Fig. 11, both agents take actions that smoothly navigate the probe toward the target standard view in the first 45 steps in their navigation. The pose errors of the two agents (marked in green) are greatly reduced to $4.63mm/6.52°$ and $3.10mm/3.66°$, respectively, and the acquired US images show high similarity with the ground truth PSL view (see Fig. 2). However, the "RL" agent mistakenly moves the probe away from the goal in the subsequent 5 steps, and reaches a location with a low confidence value in the selected ROI (step 50, $c = 0.39$). In the remaining steps, the agent moves even farther away from the goal until the end of its navigation and "misses the victory". This may be because the agent only learns to minimize the distance-to-goal and cannot interpret the shadow information, so the large acoustic shadows that suddenly appear in the image greatly affect its navigation decisions.

In contrast, the "RL+ASR" agent keeps refining the pose of the US probe in a small range after step 45, concerning both the distance-to-goal and shadow characteristics, and finally stops at a location close to the goal. Meanwhile, it can be observed from the confidence maps in Fig. 11 that the acoustic shadow area in the selected ROI of the "RL+ASR" agent is gradually decreased during the fine-tuning of the probe pose in steps 45 to 65. This shows that the shadow-aware agent has learned to maximize both the navigation reward and the auxiliary shadow reward so that it can utilize the shadow information to achieve better US acquisition results.

2) Evaluation of dual-agent collaborative navigation: Then, we evaluate the dual-agent collaborative navigation method for the integration of the RL and DL agents, as described in Section III-E. As shown in Table II, "RL+DL" and "RL+ASR+DL" denote the methods that use RL-DL collaborative navigation with the RL agent trained without and with ASR, respectively.

We first take a look at the performance of the dual-agent collaborative navigation approach when using the basic "RL"

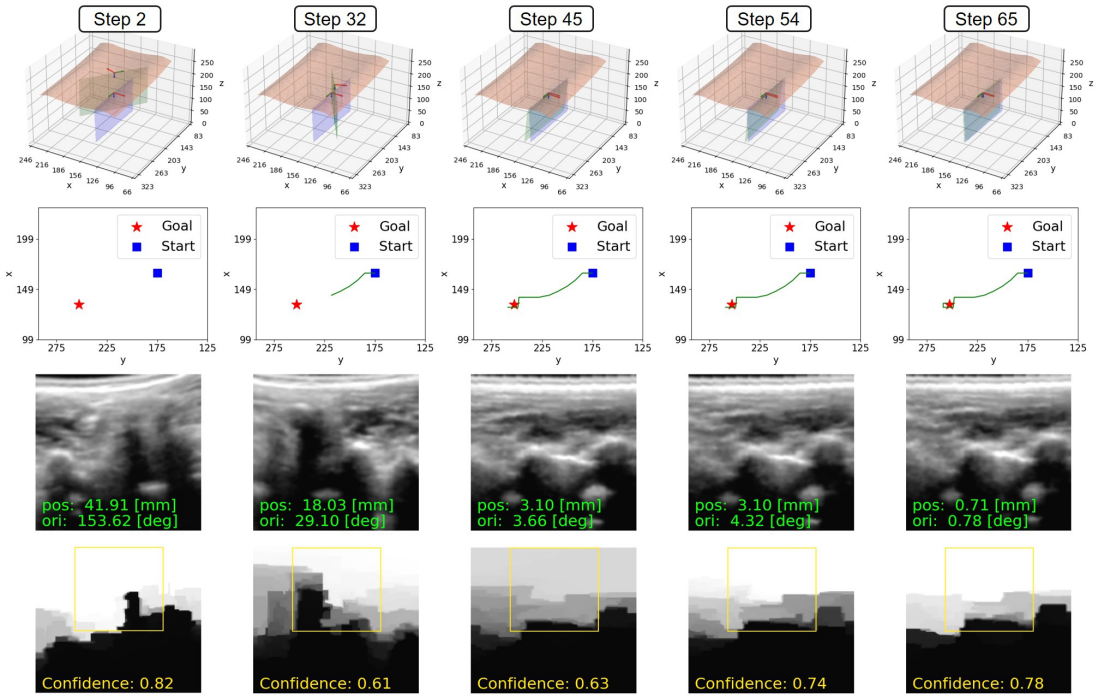

Fig. 11. Navigation trajectory of the "RL+ASR" agent toward the PSL view in the same test case as in Fig. 10. The first line shows the 3D plots of the virtual patient surface (salmon), current imaging plane (green), goal plane (blue), and the corresponding probe poses. The second line shows the top-view trajectory of the agent on the horizontal plane (green lines). The start and goal positions are indicated by a blue square and a red star, respectively. The US images are shown in the third line, with the pose errors marked in green. The confidence maps are plotted at the bottom, with the average confidence value of the selected ROI (yellow rectangle) marked in yellow.

agent. As shown in Table II (lines 1, 3), compared with the "RL" method, the "RL+DL" method can significantly reduce the final pose errors and increase the similarity between the acquired images and standard views in the intra-subject setting, especially for the PSL and PSAP view acquisitions. In the inter-subject setting, the final pose error and SSIM of the "RL+DL" method toward the PSAP and TSP views also see a large improvement over the "RL" method (see Table II, lines 5, 7), while a slight deterioration is found in the final position error during the PSL view acquisition. This may be due to the inaccurate recognition results of the DL agent and the suboptimal navigation trajectory of the RL agent trained without ASR.

Second, we compare the navigation performance of the "RL+ASR" and "RL+ASR+DL" methods to validate the effectiveness of the dual-agent collaborative navigation method when used in combination with ASR. As shown in Table II (lines 2, 4, 6, 8), the "RL+ASR+DL" method further improves over the "RL+ASR" method in the final position errors toward the standard views in both intra- and inter-subject settings. While the orientation error of the "RL+ASR+DL" method shows a slight increase by $0.52°$ compared with the "RL+ASR" method in the inter-subject setting, the final SSIM between the acquired image and the goal image of the "RL+ASR+DL" method shows a remarkable improvement over "RL+ASR" by 6%. This may be because the dual-agent framework is more sensitive to the US image content since it takes advantage of the standard view recognition results. Since the ultimate objective of our method is to acquire the standard view images that visualize the target anatomical structures, the slight deterioration of the orientation accuracy can be considered as tolerable compared with the significant improvement of image similarity.

We further investigate the effectiveness of the dual-agent collaborative navigation through qualitative analysis. As shown in Fig. 12, the standard view acquisition results of the "RL+ASR" and "RL+ASR+DL" methods are compared on example test cases. It can be observed in Fig. 12(a) that the "RL+ASR" agent takes a zig-zag path toward the PSL view in the first ~ 40 steps, and then moves aways from the goal and terminates the navigation at step 84, ending up with a pose error of $19.64mm/2.39°$ and a low SSIM of 0.25. While the "RL+ASR+DL" stops at step 47, with a pose error of $7.51mm/2.35°$ and an SSIM of 0.54, showing that using the standard view recognition results for active termination can effectively improve the navigation performance. For the PSAP view acquisition, as shown in Fig. 12(b), the "RL+ASR" agent also gradually approaches the goal at first, but takes some wrong actions in the last 20 steps and ends up with a slight deviation from the goal ($6.45mm/9.08°$). By applying the dual-agent collaboration navigation method, the stopping position is closer to goal ($3.02mm/9.08°$), and the SSIM is also increased from 0.30 to 0.49. As shown in Fig. 12(c), during the navigation toward TSP view, the "RL+ASR" agent gets trapped around the initial position and stops at step 40 with a large pose error of $24.76mm/4.81°$. In contrast, the "RL+ASR+DL" agent makes an exploration and begins a new round of search, and successfully reaches the goal at step 91, with a high accuracy of $1.68mm/4.26°$ and an SSIM of 0.72. This is because the proposed dual-agent framework can mimic

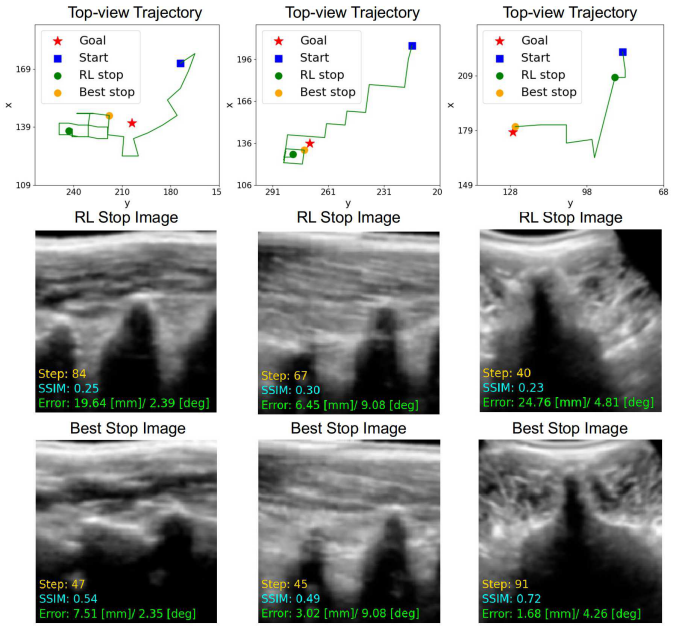

Fig. 12. (a)-(c) illustrate the PSL, PSAP, and TSP view acquisitions by the "RL+ASR" and "RL+ASR+DL" methods on example test cases. The first line shows the top-view navigation trajectories toward each target standard view (green line), with the start and goal positions indicated by a blue square and a red star. The final stopping position of the RL agent ("RL stop") and the best stop determined by dual-agent collaborative navigation ("best stop") are indicated by green and orange balls, respectively. The next two lines show the final images acquired at the RL stop and the best stop, with the corresponding termination step (yellow), final SSIM (cyan) and pose error (green).

the behavior of a sonographer to randomly reposition the probe on the patient multiple times. As a result, it can escape from bad initial positions to better search for the target anatomy and efficiently navigate the probe toward the goal within the time limit.

D. Video Demonstration

Video demonstration is available at https://youtu.be/qhtZ7-vY6M8 and https://www.bilibili.com/video/BV1A3411C78V/ for a better visualization of our results.

V. Discussion and Conclusion

In this paper, we have presented a framework that integrates RL and DL techniques for autonomous standard view acquisitions in robotic spinal sonography. The proposed RL agent can automatically control the 6-DOF movement of a US probe based on US images, and utilize the task-specific acoustic shadow information to guide the navigation. The location-sensitive DL agent for standard view recognition can jointly determine the movement of the probe to improve the navigation accuracy and efficiency. Our results in both quantitative and qualitative experiments show the effectiveness of the proposed framework, with an average navigation accuracy of $5.18mm/5.25°$ and $12.87mm/16.97°$ in the intra- and inter-subject settings, respectively.

In view of the real-world application of the framework, some additional challenges need to be addressed. First, the planned motion of the probe by our method should be executed under force monitoring and control to ensure patient safety and comfort during the robotic acquisition. Also, our simulation of probe-patient interaction has not considered the impact of contact force on the imaging results, such as tissue deformation. However, since we focus on the spinal applications, the bone structure can be roughly considered as rigid with little deformation during the scan when the force is controlled in a safe range. To generalize the proposed method to the imaging of some highly deformable human tissues (e.g., abdominal organs), the simulation environment need some modifications to include the force control by introducing additionally recorded force-image paired data. Another limitation of this work is that our simulation only considers a static patient without movement during the scan, while patient movement may cause undesired displacement of the probe in real-world US scans. Although our method can learn probe-centric navigation based on real-time US images, which has the inherent advantage of overcoming tissue movement, its robustness under patient movement has not been fully assessed. To this end, future work should also take into account the tissue motions to improve the robustness of the learned navigation policy.

Despite the challenges that need to be tackled before the method could be used in the clinical setting, our presented work has the potential to realize autonomous and intelligent robotic US imaging, and will hopefully pave the way for a promising future of US-based medical care.

Acknowledgment

The authors would like to thank Dr. Dongsheng Liu with the Department of Pain, Peking University Shenzhen Hospital, Shenzhen, China, for his help in US acquisitions.

References

[1] D. W. Rhodes and P. A. Bishop, "A review of diagnostic ultrasound of the spine and soft tissue." *Journal of Manipulative and physiological Therapeutics*, vol. 20, no. 4, pp. 267–273, 1997.

[2] D. A. Provenzano and S. Narouze, "Sonographically guided lumbar spine procedures," *Journal of Ultrasound in Medicine*, vol. 32, no. 7, pp. 1109–1116, 2013.

[3] M. Chi and A. S. Chen, "Ultrasound for lumbar spinal procedures." *Physical medicine and rehabilitation clinics of North America*, vol. 29, no. 1, pp. 49–60, 2018.

[4] R. Harel and N. Knoller, "Intraoperative spine ultrasound: application and benefits," *European Spine Journal*, vol. 25, no. 3, pp. 865–869, 2016.

[5] C. F. Baumgartner, K. Kamnitsas, J. Matthew, T. P. Fletcher, S. Smith, L. M. Koch, B. Kainz, and D. Rueckert, "Sononet: real-time detection and localisation of fetal standard scan planes in freehand ultrasound," *IEEE transactions on medical imaging*, vol. 36, no. 11, pp. 2204–2215, 2017.

[6] K.-V. Chang, M. Kara, D. C.-J. Su, E. Gürçay, B. Kaymak, W.-T. Wu, and L. Özçakar, "Sonoanatomy of the spine: A comprehensive scanning protocol from cervical to sacral region," *Medical ultrasonography*, vol. 21, no. 4, pp. 474–482, 2019.

[7] M. K. Karmakar and K. J. Chin, *Spinal Sonography and Applications of Ultrasound for Central Neuraxial Blocks*. New York, NY: McGraw-Hill Education, 2017. [Online]. Available: accessanesthesiology.mhmedical.com/content.aspx?aid=1141735352

[8] M. Karmakar, X. Li, W. Kwok, A. M. Ho, and W. Ngan Kee, "Sonoanatomy relevant for ultrasound-guided central neuraxial blocks via the paramedian approach in the lumbar region," *The British journal of radiology*, vol. 85, no. 1015, pp. e262–e269, 2012.

[9] S. Ghosh, C. Madjdpour, and K. Chin, "Ultrasound-guided lumbar central neuraxial block," *Bja Education*, vol. 16, no. 7, pp. 213–220, 2016.
[10] M. Muir, P. Hrynkow, R. Chase, D. Boyce, and D. Mclean, "The nature, cause, and extent of occupational musculoskeletal injuries among sonographers: recommendations for treatment and prevention," *Journal of Diagnostic Medical Sonography*, vol. 20, no. 5, pp. 317–325, 2004.
[11] W. A. Berg, J. D. Blume, J. B. Cormack, and E. B. Mendelson, "Operator dependence of physician-performed whole-breast us: lesion detection and characterization," *Radiology*, vol. 241, no. 2, pp. 355–365, 2006.
[12] G.-Z. Yang, B. J. Nelson, R. R. Murphy, H. Choset, H. Christensen, S. H. Collins, P. Dario, K. Goldberg, K. Ikuta, N. Jacobstein *et al.*, "Combating covid-19—the role of robotics in managing public health and infectious diseases," 2020.
[13] K. Li, Y. Xu, and M. Q.-H. Meng, "An overview of systems and techniques for autonomous robotic ultrasound acquisitions," *IEEE Transactions on Medical Robotics and Bionics*, vol. 3, no. 2, pp. 510–524, 2021.
[14] K. Li, Y. Xu, J. Wang, and M. Q.-H. Meng, "SARL*: Deep reinforcement learning based human-aware navigation for mobile robot in indoor environments," in *2019 IEEE International Conference on Robotics and Biomimetics (ROBIO)*. IEEE, 2019, pp. 688–694.
[15] S. Liu, Y. Wang, X. Yang, B. Lei, L. Liu, S. X. Li, D. Ni, and T. Wang, "Deep learning in medical ultrasound analysis: a review," *Engineering*, 2019.
[16] A. Karamalis, W. Wein, T. Klein, and N. Navab, "Ultrasound confidence maps using random walks," *Medical image analysis*, vol. 16, no. 6, pp. 1101–1112, 2012.
[17] H. Ryou, M. Yaqub, A. Cavallaro, F. Roseman, A. Papageorghiou, and J. A. Noble, "Automated 3d ultrasound biometry planes extraction for first trimester fetal assessment," in *International Workshop on Machine Learning in Medical Imaging*. Springer, 2016, pp. 196–204.
[18] C. Lorenz, T. Brosch, C. Ciofolo-Veit, T. Klinder, T. Lefevre, A. Cavallaro, I. Salim, A. T. Papageorghiou, C. Raynaud, D. Roundhill *et al.*, "Automated abdominal plane and circumference estimation in 3d us for fetal screening," in *Medical Imaging 2018: Image Processing*, vol. 10574. International Society for Optics and Photonics, 2018, p. 105740I.
[19] Y. Li, B. Khanal, B. Hou, A. Alansary, J. J. Cerrolaza, M. Sinclair, J. Matthew, C. Gupta, C. Knight, B. Kainz *et al.*, "Standard plane detection in 3d fetal ultrasound using an iterative transformation network," in *International Conference on Medical Image Computing and Computer-Assisted Intervention*. Springer, 2018, pp. 392–400.
[20] A. Alansary, L. Le Folgoc, G. Vaillant, O. Oktay, Y. Li, W. Bai, J. Passerat-Palmbach, R. Guerrero, K. Kamnitsas, B. Hou *et al.*, "Automatic view planning with multi-scale deep reinforcement learning agents," in *International Conference on Medical Image Computing and Computer-Assisted Intervention*. Springer, 2018, pp. 277–285.
[21] H. Dou, X. Yang, J. Qian, W. Xue, H. Qin, X. Wang, L. Yu, S. Wang, Y. Xiong, P.-A. Heng *et al.*, "Agent with warm start and active termination for plane localization in 3d ultrasound," in *International Conference on Medical Image Computing and Computer-Assisted Intervention*. Springer, 2019, pp. 290–298.
[22] C. Hennersperger, B. Fuerst, S. Virga, O. Zettinig, B. Frisch, T. Neff, and N. Navab, "Towards mri-based autonomous robotic us acquisitions: a first feasibility study," *IEEE transactions on medical imaging*, vol. 36, no. 2, pp. 538–548, 2016.
[23] Q. Huang, B. Wu, J. Lan, and X. Li, "Fully automatic three-dimensional ultrasound imaging based on conventional b-scan," *IEEE transactions on biomedical circuits and systems*, vol. 12, no. 2, pp. 426–436, 2018.
[24] G. Ning, X. Zhang, and H. Liao, "Autonomic robotic ultrasound imaging system based on reinforcement learning," *IEEE Transactions on Biomedical Engineering*, 2021.
[25] N. Siddiqui, E. Yu, S. Boulis, and K. E. You-Ten, "Ultrasound is superior to palpation in identifying the cricothyroid membrane in subjects with poorly defined neck landmarks: a randomized clinical trial," *Anesthesiology*, vol. 129, no. 6, pp. 1132–1139, 2018.
[26] C. Nadeau, H. Ren, A. Krupa, and P. Dupont, "Intensity-based visual servoing for instrument and tissue tracking in 3d ultrasound volumes," *IEEE Transactions on Automation Science and Engineering*, vol. 12, no. 1, pp. 367–371, 2014.
[27] R. Nakadate, J. Solis, A. Takanishi, E. Minagawa, M. Sugawara, and K. Niki, "Implementation of an automatic scanning and detection algorithm for the carotid artery by an assisted-robotic measurement system," in *2010 IEEE/RSJ International Conference on Intelligent Robots and Systems*. IEEE, 2010, pp. 313–318.
[28] R. Droste, L. Drukker, A. T. Papageorghiou, and J. A. Noble, "Automatic probe movement guidance for freehand obstetric ultrasound," in *International Conference on Medical Image Computing and Computer-Assisted Intervention*. Springer, 2020, pp. 583–592.
[29] A. Hussein, M. M. Gaber, E. Elyan, and C. Jayne, "Imitation learning: A survey of learning methods," *ACM Computing Surveys (CSUR)*, vol. 50, no. 2, pp. 1–35, 2017.
[30] F. Milletari, V. Birodkar, and M. Sofka, "Straight to the point: reinforcement learning for user guidance in ultrasound," in *Smart Ultrasound Imaging and Perinatal, Preterm and Paediatric Image Analysis*. Springer, 2019, pp. 3–10.
[31] H. Hase, M. F. Azampour, M. Tirindelli, M. Paschali, W. Simson, E. Fatemizadeh, and N. Navab, "Ultrasound-guided robotic navigation with deep reinforcement learning," *arXiv preprint arXiv:2003.13321*, 2020.
[32] K. Li, J. Wang, Y. Xu, H. Qin, D. Liu, L. Liu, and M. Q.-H. Meng, "Autonomous navigation of an ultrasound probe towards standard scan planes with deep reinforcement learning," in *2021 IEEE International Conference on Robotics and Automation (ICRA)*, 2021, pp. 8302–8308.
[33] A. Lasso, T. Heffter, A. Rankin, C. Pinter, T. Ungi, and G. Fichtinger, "Plus: Open-source toolkit for ultrasound-guided intervention systems," *IEEE Transactions on Biomedical Engineering*, vol. 61, no. 10, pp. 2527–2537, 2014.
[34] Q.-H. Huang, Y.-P. Zheng, M.-H. Lu, and Z. Chi, "Development of a portable 3d ultrasound imaging system for musculoskeletal tissues," *Ultrasonics*, vol. 43, no. 3, pp. 153–163, 2005.
[35] V. Mnih, K. Kavukcuoglu, D. Silver, A. A. Rusu, J. Veness, M. G. Bellemare, A. Graves, M. Riedmiller, A. K. Fidjeland, G. Ostrovski *et al.*, "Human-level control through deep reinforcement learning," *nature*, vol. 518, no. 7540, pp. 529–533, 2015.
[36] D. P. Kingma and J. Ba, "Adam: A method for stochastic optimization," *arXiv preprint arXiv:1412.6980*, 2014.
[37] K. Simonyan and A. Zisserman, "Very deep convolutional networks for large-scale image recognition," *arXiv preprint arXiv:1409.1556*, 2014.
[38] J. Deng, W. Dong, R. Socher, L.-J. Li, K. Li, and L. Fei-Fei, "Imagenet: A large-scale hierarchical image database," in *2009 IEEE conference on computer vision and pattern recognition*. Ieee, 2009, pp. 248–255.

Keyu Li received the B.Eng. degree in communication engineering from Harbin Institute of Technology (HIT), Weihai, China, in 2019. She is currently pursuing the Ph.D. degree with the Department of Electronic Engineering, The Chinese University of Hong Kong (CUHK), Hong Kong SAR, China. Her research interests include artificial intelligence in robot decision-making, medical robotics, and medical imaging applications, with a focus on autonomous robotic ultrasound systems, supervised by Prof. Max Q.-H, Meng.

Ms. Li is an awardee of the Hong Kong PhD Fellowship Scheme (HKPFS) since 2019.

Yangxin Xu received the B.Eng. degree in electrical engineering and its automation from Harbin Institute of Technology (HIT), Weihai, Shandong, China, in 2017, and the Ph.D. degree from the Department of Electronic Engineering, The Chinese University of Hong Kong (CUHK), Hong Kong SAR, China, in 2021. His research focuses on magnetic actuation and localization methods and hardware implementation for active wireless robotic capsule endoscopy, supervised by Prof. Max Q.-H, Meng.

Mr. Xu received the Best Conference Paper from the 2018 IEEE International Conference on Robotics and Biomimetics (ROBIO), Kuala Lumpur, Malaysiain, in 2018.

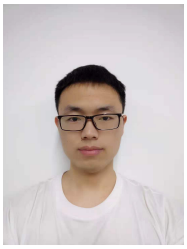

Jian Wang received the Master's degree in biomedical engineering from Shenzhen University, China, in 2021. His research interest is in the application of deep learning to ultrasound images, with a particular focus on the breast and thyroid glands. He has published journal papers in Medical Image Analysis and conference papers in MICCAI.

Dong Ni received the bachelor's and master's degrees in biomedical engineering from Southeast University, Nanjing, China, in 2000 and 2003, respectively, and the Ph.D. degree in computer science and engineering from The Chinese University of Hong Kong, Hong Kong, in 2009. From 2009 to 2010, he was a Postdoctoral Fellow of the School of Medicine, University of North Carolina at Chapel Hill, USA. Since 2010, he has been with Shenzhen University, China, where he is currently a Professor and the Associate Dean of the Health Science Center, School of Biomedical Engineering. He founded the Medical Ultrasound Image Computing (MUSIC) Laboratory, Shenzhen University. His research interests include ultrasound image analysis, image guided surgery, and pattern recognition.

Li Liu received the Ph.D. degree in biomedical engineering from the University of Bern, Switzerland, in 2016. He joined as an Assistant Professor with the Health Science Center, School of Biomedical Engineering, Shenzhen University, in 2016. He is currently a Research Assistant Professor with the Department of Electronic Engineering, The Chinese University of Hong Kong. His current research interests include surgical robotics and navigation, ultrasonic/photoacoustic guided surgical intervention, and AI empowered interventions.

Dr. Liu was a recipient of the Distinguished Doctorate Dissertation Award from the Best Paper Award of IEEE ICIA, in 2009, the MICCAI Student Travel Award, in 2014, and the Swiss Institute of Computer Assisted Surgery, in 2016. He served as a Publication Chair for many international conferences, including a Publication Chair of IEEE ICIA 2017 and 2018 and a Program Chair of IEEE ROBIO 2019. He served as a reviewer for several journals and program.

Max Q.-H. Meng received the Ph.D. degree in electrical and computer engineering from the University of Victoria, Victoria, BC, Canada, in 1992.

He was with the Department of Electrical and Computer Engineering, University of Alberta, Edmonton, AB, Canada, where he served as the Director of the Advanced Robotics and Teleoperation Laboratory, holding the positions of Assistant Professor, Associate Professor, and Professor in 1994, 1998, and 2000, respectively. In 2001, he joined The Chinese University of Hong Kong, where he served as the Chairman of the Department of Electronic Engineering, holding the position of Professor. He is affiliated with the State Key Laboratory of Robotics and Systems, Harbin Institute of Technology, and is the Honorary Dean of the School of Control Science and Engineering, Shandong University, China. He is currently with the Department of Electronic and Electrical Engineering, Southern University of Science and Technology, on leave from the Department of Electronic Engineering, The Chinese University of Hong Kong, Hong Kong SAR, China, and also with the Shenzhen Research Institute of the Chinese University of Hong Kong, Shenzhen, China. His research interests include robotics, medical robotics and devices, perception, and scenario intelligence. He has published about 600 journal and conference papers and led more than 50 funded research projects to completion as PI.

Dr. Meng is an elected member of the Administrative Committee (AdCom) of the IEEE Robotics and Automation Society. He is a recipient of the IEEE Millennium Medal, a fellow of the Canadian Academy of Engineering, and a fellow of HKIE. He has served as an editor for several journals and also as the General and Program Chair for many conferences, including the General Chair of IROS 2005 and the General Chair of ICRA 2021.